Research Square

Preprints are preliminary reports that have not undergone peer review.
They should not be considered conclusive, used to inform clinical practice,
or referenced by the media as validated information.

Inverse identification of parameters and decomposition analysis of influencing factors for the coupled variable-friction model at the Ti6Al4V cutting interface

Chengsong Ma

134648110230163.com

Guizhou Normal University https://orcid.org/0009-0006-4796-6904

Xinxin Zhang

Yang Xin

Zichuan Zou

Research Article

Keywords: Ti6Al4V, Variable Coefficient of Friction, Coupled Simulation, Contact State

Posted Date: September 10th, 2026

DOI: https://doi.org/10.21203/rs.3.rs-10899569/v1

License: This work is licensed under a Creative Commons Attribution 4.0 International License.
Read Full License

Inverse identification of parameters and decomposition analysis of influencing factors for the coupled variable-friction model at the Ti6Al4V cutting interface

Chengsong Ma [a], Xinxin Zhang [a], Yang Xin[a], Zichuan Zou [a,*]

a School of Mechanical and Electrical Engineering, Guizhou Normal University, Guiyang 550025, China

*** Corresponding author: Zichuan Zou**

E-mail: zichuan@gznu.edu.cn

Abstract: Tool-chip friction in Ti6Al4V cutting evolves with contact temperature, normal contact stress, and relative sliding velocity, making a single constant coefficient insufficient to describe the changing contact state. A coupled variable-friction formulation incorporating these three dependencies was therefore implemented in a two-dimensional orthogonal-cutting finite element model through the Abaqus VFRIC subroutine. Its unknown parameters were identified through inverse calibration within an Abaqus-Python-Isight co-simulation loop, using the difference between simulated and experimentally measured main cutting forces as the optimization objective. Cutting experiments were then used to assess the model together with a conventional Coulomb formulation by comparing force predictions and chip morphology. Relative to the Coulomb model, whose average cutting-force error was 20.8%, the coupled formulation reduced the error to 5.55% while reproducing the characteristic serrated chips observed for Ti6Al4V. Three reduced formulations were subsequently introduced by removing one state dependence at a time. The ablation results showed the largest deterioration in cutting-force prediction when the sliding-velocity term was suppressed. Removing the temperature or normal-stress dependence had a smaller effect on the mean force level but altered the predicted chip response through changes in material softening, interfacial adhesion, and local shear-traction distribution. These results support the use of the three state variables as complementary inputs for describing the evolving Ti6Al4V tool-chip interface.

Keywords: Ti6Al4V; Variable Coefficient of Friction; Coupled Simulation; Contact State

1. Introduction

Ti6Al4V remains an important alloy for aerospace and biomedical applications because its low density, high specific strength, corrosion resistance, and elevated-temperature capability provide a favorable

combination of service properties[1]. These advantages are accompanied by substantial difficulties during machining. Heat is removed inefficiently from the deformation zone because of the low thermal conductivity of the alloy, while its chemical affinity and relatively low elastic modulus favor adhesion and severe local loading at the rake face[2]. The tool-chip interface consequently contributes appreciably to both cutting resistance and heat generation. Of particular relevance to friction modeling is the strong spatial variation within this interface. As the chip moves over the rake face, temperature, normal contact stress, and relative sliding velocity do not remain uniform but vary with contact position[3]. Representing the entire region by a single prescribed friction coefficient can therefore obscure these local differences and reduce the accuracy of predicted cutting force, chip segmentation, and thermomechanical fields[4].

The frictional behavior of machining interfaces has been investigated through direct tribological testing, inverse identification, and numerical modeling[5]. Direct tests can provide useful friction data under controlled conditions, but conventional tribometers cannot simultaneously reproduce several characteristics of the cutting interface, such as contact pressures on the order of 1–3 GPa, continuous formation of fresh surfaces, intense plastic deformation, and rapid temperature evolution[6]. Inverse approaches based on measurable cutting responses can represent the actual machining process more closely, although the identified parameters generally correspond to an effective response of the contact region rather than the full local variation between sticking and sliding zones[7]. Finite element analysis offers a complementary route because local stress, temperature, contact, and material-response variables can be evaluated within the same computational framework. Its predictive reliability, however, remains strongly dependent on both the physical adequacy of the imposed friction law and the robustness of the parameters used in that law[8].

Among the available interface descriptions, the Coulomb model remains widely used because of its simple formulation, in which frictional shear stress is proportional to normal contact stress[9]. Such a representation is computationally convenient but does not describe the saturation of interfacial shear stress or the transition between sticking and sliding that develops under severe machining conditions. Shet and Deng addressed this limitation by restricting the maximum interfacial shear stress according to the shear strength of the workpiece material [10], although the friction coefficient itself remained independent of the evolving local state. Temperature dependence was subsequently introduced into thermomechanical descriptions of the cutting interface, allowing interfacial temperature to be related to contact length and force distribution[11]. Sticking-sliding formulations, such as the Zorev model, further distinguish regions

of the interface according to whether the local shear stress reaches its limiting value[12]. In the sticking region, relative motion is strongly restricted and the shear stress approaches saturation, whereas in the sliding region the shear stress varies with the local normal contact stress. A schematic representation of these two contact regimes is given in Fig. 1.

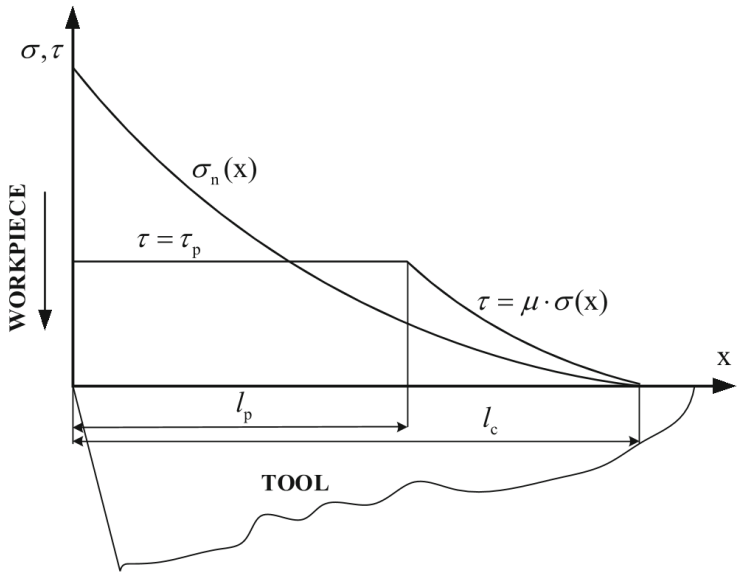


Fig. 1 Schematic illustration of the stress distribution in the sticking and sliding zones at the tool-chip interface

The relative motion of the chip also changes considerably along the rake face. Velocity-dependent friction descriptions have therefore been used to account for the increase in sliding motion away from the strongly constrained contact region[13]. Within a sliding region, the local friction state can additionally be related to the ratio between interfacial shear and normal tractions[14]. Although these formulations capture useful aspects of the interface, individual models often emphasize one state variable at a time [15]. This separation is particularly restrictive for Ti6Al4V because pressure, temperature, and sliding velocity evolve concurrently. Temperature changes material strength, normal pressure modifies the local contact and adhesion state, and sliding velocity influences both interfacial shearing and frictional heat generation. During segmented-chip formation these effects develop together with the deformation field; treating them independently may therefore reproduce one cutting response while remaining inadequate for another[16].

The present work addresses this issue by treating contact temperature, normal contact stress, and relative sliding velocity as simultaneous state inputs to the friction law. The resulting coupled formulation is introduced into a two-dimensional orthogonal-cutting model through the VFRIC user subroutine in Abaqus/Explicit, allowing the friction condition to be updated as the local interface variables change. Its coefficients are not assigned in advance; instead, they are obtained from measured main cutting forces through an Abaqus-Python-Isight inverse-identification procedure. The identified formulation is

subsequently examined against experimental observations and a constant-coefficient Coulomb model using the main cutting force and chip morphology as response quantities. To examine the role of each explicit dependence, three reduced formulations are also constructed by suppressing the temperature-, normal-contact-stress-, and sliding-velocity-dependent terms individually. Each reduced model is assessed against the corresponding cutting responses so that the contribution of the omitted term can be distinguished from the behavior of the complete coupled formulation. The overall procedure is summarized in Fig. 2.

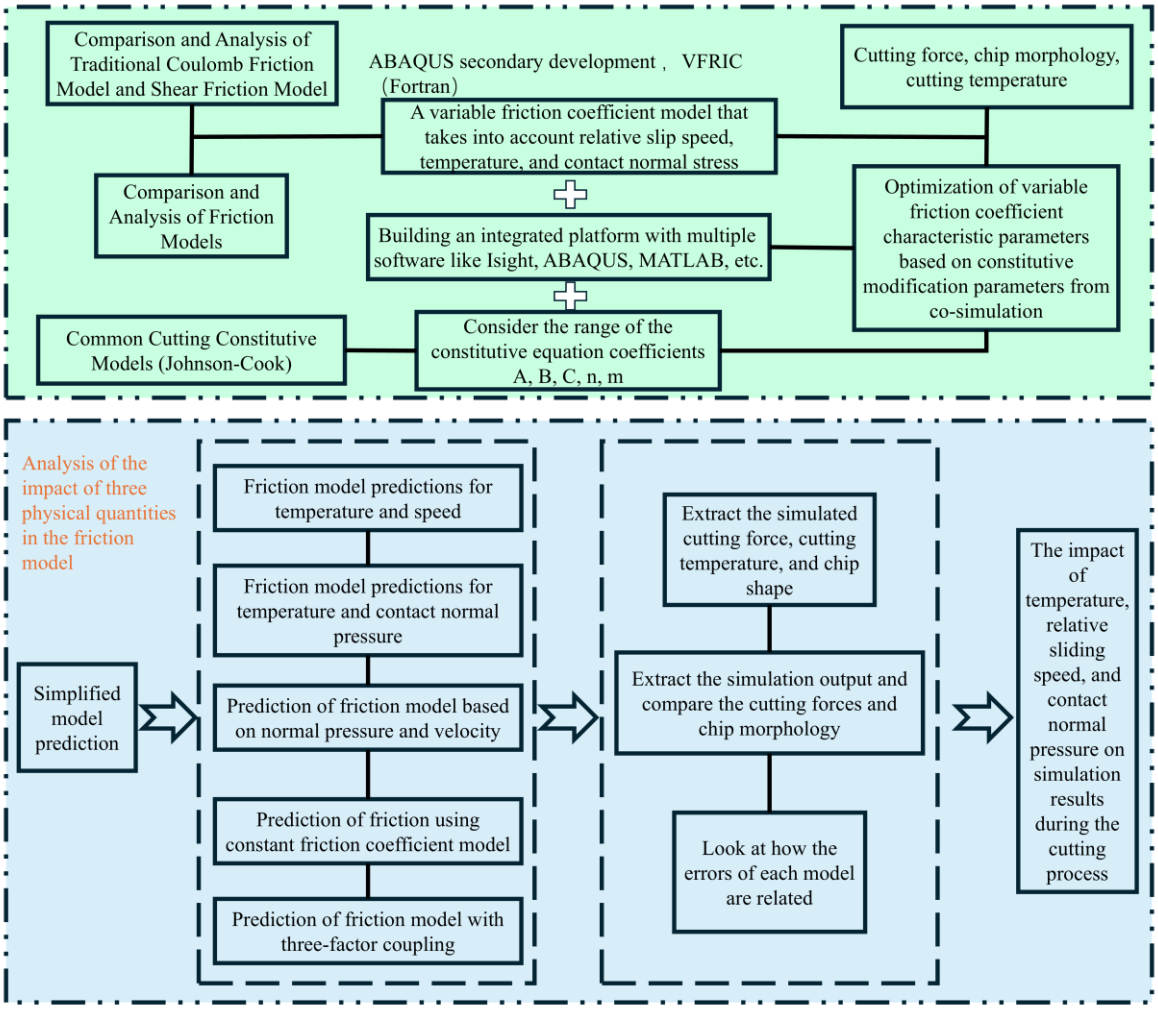


Fig. 2 Overall research workflow

2. Construction and Numerical Implementation of the Coupled Variable Friction Coefficient Model

2.1 Construction of the Multi-Factor Coupled Variable Friction Coefficient Model

The friction condition at the tool-chip interface is governed by a highly nonuniform thermomechanical state. In particular, the local contact pressure, sliding condition, and temperature vary continuously along the rake face and during chip formation. A friction formulation intended for cutting simulation should therefore describe not only the magnitude of the interfacial shear traction but also its evolution with these local state variables. In the present model, a Coulomb-type relation is retained as the basic description of sliding resistance, following the classical friction formulation introduced by Merchant[17]:

$$\tau_f = \mu\sigma_n \tag{1}$$

where τ_f denotes the frictional shear stress, σ_n is the normal contact stress, and μ is the friction coefficient. A purely proportional relation, however, permits the interfacial shear stress to increase indefinitely with normal pressure. Such behavior is not suitable for representing the transition from sliding to highly constrained contact under severe machining conditions. The shear traction is therefore restricted by a limiting interfacial shear stress, giving the following piecewise contact relation:

$$\tau_f = \begin{cases} \mu\sigma_n, \mu\sigma_n < \tau_s \\ \tau_s, \mu\sigma_n \geq \tau_s \end{cases} \tag{2}$$

Here, σ_n denotes the limiting shear stress at the tool-chip interface. Equation (2) separates two mechanical responses within the same contact law. When $\mu\sigma_n < \tau_s$, the local shear traction remains pressure dependent; once the Coulomb traction reaches the limiting value, further increases in normal contact stress no longer produce a proportional increase in interfacial shear stress. This formulation provides the traction constraint used in the coupled friction model developed below.

To introduce pressure dependence into the friction coefficient itself, the contact behavior is considered from an adhesion-based perspective. Metallic contact occurs over a collection of localized junctions forming the real contact area rather than over the complete nominal interface[18]. Tangential resistance may consequently contain contributions from both shearing of these junctions and ploughing associated with local surface interaction[19]. The total friction force is expressed as:

$$F = F_j + F_l \tag{3}$$

where F, F_j, and F_l denote the total friction force, the shear contribution, and the ploughing contribution, respectively. For the idealized elastic-plastic contact considered in the present formulation, the ploughing contribution is assumed to be small compared with the adhesive shear contribution. The resulting friction force can therefore be related to the real contact area and the limiting shear strength of the adhesive junctions as:

$$F = A_z \tau_b = \frac{N}{\sigma_S} \tau_b \tag{4}$$

The corresponding friction coefficient becomes:

$$\mu = \frac{F}{N} = \frac{\tau_b}{\sigma_s} \tag{5}$$

where A_z is the real contact area, N is the normal load, τb denotes the limiting shear strength of the adhesive junctions, and σ_s represents the compressive yield strength. Equations (4) and (5) indicate that the friction coefficient depends on the mechanical state of the contacting material and therefore need not remain constant as the interface pressure changes.

The pressure contribution is introduced by considering the evolution of the limiting interfacial shear strength under local compression. Below the compressive-yield level, τ_b is treated as approximately insensitive to further changes in normal stress. Beyond this level, the limiting shear strength continues to increase, but at a slower rate than the normal contact stress. This response is represented by

$$\tau_b \propto \begin{cases} const, & \sigma_n \leq \sigma_b \\ \sigma_n^m, & \sigma_n > \sigma_b \end{cases} \tag{6}$$

where m is a constant satisfying 0< m <1. Combining this pressure response with Eq. (5) gives the corresponding dependence of the friction coefficient on normal contact stress:

$$\mu \propto \frac{1}{\sigma_n^k} \tag{7}$$

where $k = 1 - m$ and $0 < k < 1$. Equation (7) provides the pressure-dependent component of the present friction law. Its principal role is to prevent a single prescribed value of μ from being applied over regions of the rake face that experience substantially different normal contact stresses.

Pressure variation alone does not fully characterize the cutting interface. Relative sliding velocity and contact temperature also evolve during chip motion and have been reported to influence the friction coefficient[20]. Their contributions are introduced through the following functional relationships::

$$\mu \propto e^{-av} \tag{8}$$

$$\mu \propto 1 - \left(\frac{T}{T_m}\right)^b \tag{9}$$

In Eqs. (8) and (9), v denotes the relative sliding velocity, T is the average rake-face temperature, T_m is the melting temperature of the workpiece, and a and b are the corresponding constants. The two relations introduce separate velocity and thermal responses into the friction coefficient.

In addition to changing the friction coefficient, temperature alters the mechanical strength that constrains the maximum interfacial shear traction. The limiting shear stress is related to the shear yield strength of the workpiece material[21].

$$\tau_{max} = \frac{1}{\sqrt{3}}\sigma_y \tag{10}$$

where σ_y denotes the yield strength of Ti6Al4V. Because substantial heating occurs during machining, the variation of σy with temperature must be included in the traction limit[22]. The temperature-dependent relation proposed by Komanduri and Hou [23] is therefore adopted::

$$\sigma_y = 955.3 - 0.943T \tag{11}$$

The relation between the workpiece shear strength and the limiting shear stress also varies with the friction state. According to Zhang et al.[24], the limiting interfacial shear stress differs from the material shear yield strength when the friction coefficient is below the specified transition value, whereas the two become equivalent above this threshold. Incorporating this condition together with the fitted relationship reported for the interface[25] gives:

$$\tau_{max} = \begin{cases} [0.497 + 0.507(\mu - 0.3)] \times (955.3 - 0.943T), \mu < 0.48 \\ \frac{1}{\sqrt{3}}(955.3 - 0.943T), \mu \geq 0.48 \end{cases} \tag{12}$$

Equations (7)-(12) define different functions within the same interface description rather than independent friction models. The normal contact stress controls the pressure-sensitive contribution to μ; relative sliding velocity introduces the dependence on local chip motion; and temperature affects both the friction coefficient and the upper bound of the interfacial shear traction. These quantities are therefore evaluated simultaneously so that the friction condition can respond to the instantaneous thermomechanical state of the tool-chip interface.

Combining the three state-variable dependencies with the limiting-shear-stress constraint yields the multi-factor coupled variable-friction formulation used in this study:

$$\begin{cases} \mu = ae^{-bv}\left[1 - \left(\frac{T}{T_m}\right)^c\right]/\sigma_n^d \\ \tau = min(\mu\sigma_n, \tau_{max}) \end{cases} \tag{13}$$

where a, b, c, d are the model parameters to be identified, with $0 < d < 1$. Unlike a constant-coefficient formulation, Eq. (13) permits the friction coefficient to vary with normal contact stress, relative sliding velocity, and temperature while simultaneously restricting the resulting shear traction through τmax. The values of the four parameters are not prescribed empirically in advance but are subsequently determined from the cutting-force response through the inverse-identification procedure described in Section 4.

2.2 Implementation of the Coupled Friction Model through the VFRIC Subroutine

The built-in contact models in Abaqus generally rely on predefined friction formulations, making it difficult to directly implement a user-defined friction law that simultaneously accounts for contact temperature, normal contact stress, and relative sliding velocity. Therefore, the VFRIC interface provided in Abaqus/Explicit was employed to implement the proposed coupled variable-friction model. The execution procedure of the VFRIC subroutine is illustrated in Fig. 3. At the beginning of each analysis increment, the Abaqus main program first performs contact detection. Once contact is detected between the tool and the workpiece, the main program passes the variables characterizing the current contact state, including normal contact stress, nodal temperature, and relative sliding velocity, to the VFRIC subroutine. Based on the proposed coupled friction law, the subroutine calculates the interfacial shear stress for the current increment. It returns the calculated value to the Abaqus main program for subsequent contact calculations and dynamic equilibrium solution. Through this procedure, the frictional state at the tool-chip interface can be dynamically updated in accordance with the evolving local thermomechanical condition.

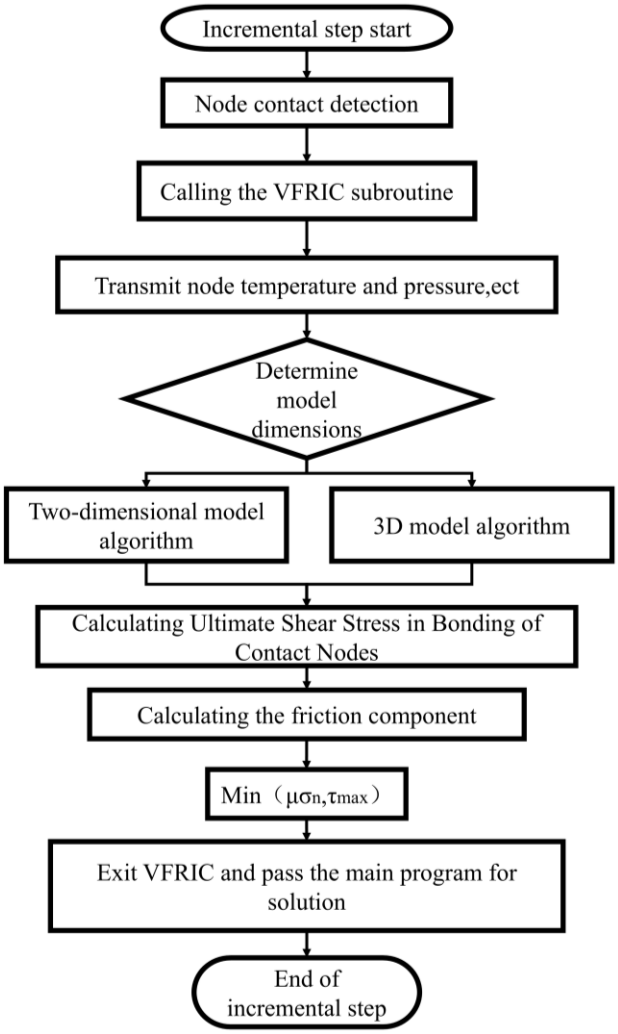


Fig. 3 VFRIC subroutine calling procedure

3. Finite Element Model of Two-Dimensional Orthogonal Cutting of Ti6Al4V

3.1 Workpiece Material Properties

The workpiece material was Ti6Al4V. Its chemical composition and physical and mechanical properties are listed in Table 1 and Table 2, respectively.

Table 1 Chemical composition of Ti6Al4V.（wt.%）[26]

Al	V	Fe	N+O	Ti
4.83-6.85	2.31-4.2	0.17	0.19（max）	Balance

Table 2 Material properties of Ti6Al4V. [27]

Material property	Value
Density (kg/m^3)	4500

Young's modulus（GPa）	112
Poisson's ratio	0.34
Thermal conductivity（W/(m*K)）	7.6
Specific heat capacity (J/Kg/K)	611
Melting point (°C)	1650

3.2 Constitutive Model

During Ti6Al4V cutting, the material within the primary and secondary deformation regions is subjected to large plastic deformation while the strain rate and temperature change simultaneously[28]. The resulting loading state differs substantially from that represented by conventional quasi-static material tests[29]. Consequently, the constitutive law used in the finite element model must be capable of updating the flow stress in response to the evolving deformation and thermal state.

Several constitutive formulations have been applied to machining simulations, including the Zerilli-Armstrong model[30], the Bodner-Partom model[31], and the Johnson-Cook (J-C) model[32]. For the present analysis, the J-C formulation was selected because it represents strain hardening, strain-rate sensitivity, and thermal softening through separate terms within a single flow-stress expression[33]. This structure enables the material strength to vary directly with the local equivalent plastic strain, plastic strain rate, and temperature calculated during the cutting simulation.

$$\sigma = (A + B\varepsilon^{n})\left[1 + C\ln\left(\frac{\dot{\varepsilon}}{\dot{\varepsilon}_0}\right)\right]\left[1 - \left(\frac{1 - T_r}{T_m - T_r}\right)^{m}\right] \tag{14}$$

Equation (14) can be interpreted in terms of three contributions to the instantaneous flow stress. The first term describes the increase in material strength associated with accumulated plastic deformation, the second accounts for the influence of deformation rate, and the final term represents the reduction in flow stress caused by thermal softening. Their combined action therefore allows the constitutive response to evolve continuously as the thermomechanical state changes during chip formation.

In Eq. (14), ε and $\dot{\varepsilon}$ denote the equivalent plastic strain and equivalent plastic strain rate, respectively, while $\dot{\varepsilon}_0$ is the reference strain rate. T represents the instantaneous deformation temperature, T_r is the reference temperature taken as room temperature, and T_m is the melting temperature of Ti6Al4V. The parameters A and B define the reference yield response and strain-hardening contribution, respectively; n controls the evolution of strain hardening, C characterizes strain-rate sensitivity, and m governs thermal softening. The J-C parameters adopted for Ti6Al4V in the present finite element model are

summarized in Table 3.

Table 3 J-C constitutive model coefficients of Ti6Al4V[25]

A (MPa)	B (MPa)	n	C	m	$\dot{\varepsilon}_0$(s^{-1})	T_m(℃)	T_r(℃)
782.7	498.4	0.28	0.028	1	1E-5	1630	20

3.3 Damage Model and Failure Criterion

A constitutive law alone cannot reproduce chip separation because the finite element model also requires a criterion for the onset and accumulation of material damage[34]. Different damage-initiation approaches, including ductile- and shear-based criteria, have been used in machining simulations[35]. For the present Ti6Al4V model, the Johnson-Cook damage law was employed to describe material failure under the large deformation and high strain-rate conditions associated with chip formation[36].

The formulation includes the influence of stress state following the fracture-mechanics considerations represented in the Hancock-Mackenzie framework[37]. Damage is accumulated incrementally as plastic deformation proceeds, and material separation occurs after the prescribed failure condition has been satisfied[38]. The accumulated damage variable is calculated from:

$$\omega = \sum \frac{\triangle \varepsilon^{pl}}{\varepsilon_f^{pl}} \tag{15}$$

In Eq. (15), ω represents the cumulative damage state of a material point. The quantity $\triangle \varepsilon^{pl}$ is the equivalent plastic-strain increment accumulated during the current increment, whereas ε_f^{pl} denotes the equivalent plastic strain required for failure under the corresponding local loading state. Damage therefore develops progressively as plastic deformation proceeds rather than being imposed as an instantaneous separation condition. When the accumulated value of ω reaches the prescribed failure limit, the material point is regarded as having lost its load-carrying capacity, providing the criterion used to represent chip separation in the finite element calculation. The failure strain ε_f^{pl} is evaluated from the Johnson-Cook damage relation:

$$\varepsilon_f^{pl} = [d_1 + d_2 exp(d_3\sigma^*)][1 + d_4 \ln \varepsilon^*]\left[1 + d_5\left(\frac{T - T_r}{T_m - T_r}\right)\right] \tag{16}$$

where σ^* denotes the stress triaxiality, T is the cutting temperature, and d_1–d_5 are the J-C damage parameters. The values adopted for Ti6Al4V are listed in Table 4.

Table 4 J-C damage failure parameters of Ti6Al4V[25]

d_1	d_2	d_3	d_4	d_5

-0.09	0.25	-1.5	0.014	3.87

3.4 Geometric Model, Mesh Generation, and Boundary Conditions

A two-dimensional finite element model of orthogonal cutting of Ti6Al4V was established, as illustrated in Fig. 4. The tool had a rake angle of 14° and a cutting-edge radius of 20 μm and was modeled as a rigid body. The workpiece was 2 mm in length L and 1 mm in height H. To balance computational accuracy in the cutting zone with overall computational efficiency, the workpiece was partitioned along a line located 0.7 mm above its lower surface, and the element size in the upper cutting region was set to 0.005 mm. A small initial clearance was introduced between the tool tip and the workpiece to mitigate mesh distortion caused by abrupt tool-workpiece contact at the beginning of the simulation. The boundary conditions of the model and the definition of the cutting depth are also illustrated in Fig. 4.

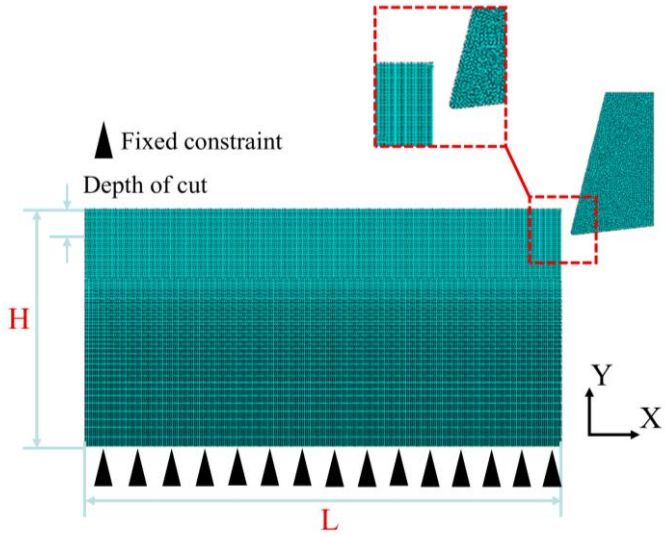


Fig. 4 Schematic illustration of the simulation setup

4. Inverse Identification and Experimental Validation of Coupled Friction Model Parameters

Friction-model parameters are generally determined through pin-on-disc or pin-on-cylinder tests by fitting measured normal and tangential forces. However, owing to the limited loading capacity of the experimental equipment, the normal contact stress attainable in these tests is typically much lower than that

encountered during actual cutting. Consequently, the resulting friction parameters cannot reliably characterize the actual frictional behavior at the tool-chip interface. To overcome this limitation, the Abaqus finite element model of the cutting process was coupled with the Isight optimization platform in the present study. The parameters of the coupled variable-friction model were inversely identified through co-simulation and iterative optimization by minimizing the discrepancy between the simulated and experimentally measured main cutting forces.

4.1 Experimental Design and Acquisition of Response Data

The experimental cutting tests were carried out on a C6316HK CNC lathe using the arrangement shown in Fig. 5. A Ti6Al4V cylindrical bar with dimensions of Φ80 mm × 200 mm was first machined with circumferential grooves, leaving annular bosses for the orthogonal-cutting tests. Main cutting force was recorded with a Kistler 9257B dynamometer installed beneath the tool holder.

Tool wear was controlled by replacing the cutting tool before each group of tests. Three repeated measurements were performed for every cutting condition, and their arithmetic mean was used as the corresponding main cutting-force response. The cutting geometry used in the experiments was consistent with that prescribed in the finite element model: the rake angle was 14°, the clearance angle was 6°, and the cutting-edge radius was 20 μm. The complete test matrix and the measured main cutting forces are reported in Table 5.

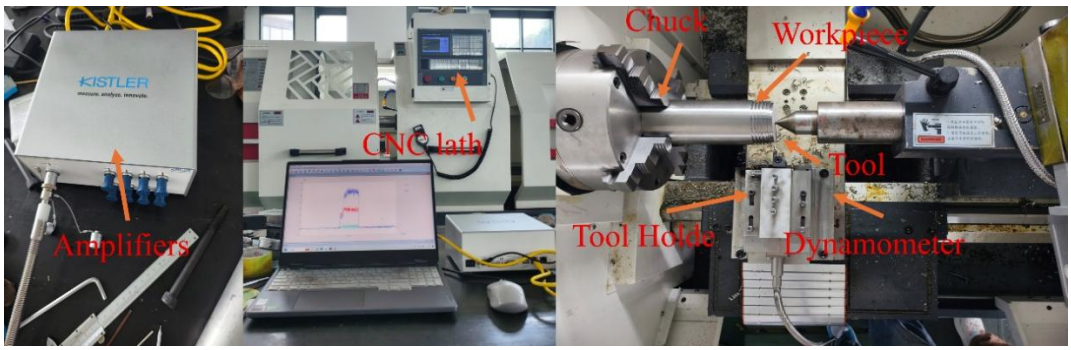


Fig. 5 Experimental setup

Table 5 Orthogonal cutting test plan and measured main cutting forces for Ti6Al4V.

Test No.	Cutting speed (m/min)	Feed rate (mm/rev)	Depth of cut (mm)	Width of cut (mm)	Main cutting force（N）
1	60	0.15	0.2	3	357.7
2	60	0.20	0.2	3	456.2
3	60	0.25	0.2	3	505.6

4	80	0.15	0.2	3	372.4
5	80	0.20	0.2	3	450.8
6	80	0.25	0.2	3	517.1
7	100	0.15	0.2	3	353.5
8	100	0.20	0.2	3	423.5
9	100	0.25	0.2	3	523.8

4.2 Inverse Identification of Model Parameters Based on Co-Simulation

The four unknown parameters of the coupled variable-friction model were calibrated through a closed-loop inverse-identification procedure based on the experimentally measured main cutting forces. An Abaqus-Python-Isight co-simulation framework was established so that each candidate parameter set could be automatically evaluated under the cutting conditions considered in this study.

During each optimization iteration, the multi-island genetic algorithm implemented in Isight generated a candidate parameter vector (a,b,c,d). The corresponding values were passed to a Python script, which updated the friction-model parameters in the two-dimensional thermomechanically coupled Abaqus cutting model, submitted the analysis job, and extracted the predicted main cutting force after completion of the simulation. The numerical response was then transferred to MATLAB together with the corresponding experimental value, and the fitness of the candidate parameter set was evaluated from the mean squared relative error between the simulated and measured cutting forces. The calculated fitness was returned to Isight and used to generate the subsequent population, thereby completing one iteration of the inverse-identification loop.

The optimization problem was formulated as follows:

$$Find:\ (a,\ b,\ c,\ d) \tag{17}$$

$$Min:\ E = \frac{1}{N}\sum_{1}^{N}\left(\frac{F_{FEM}}{F_{EXP}} - 1\right)^2 \tag{18}$$

$$Subjectto:\ \begin{cases} a_{min} \le a \le a_{max} \\ b_{min} \le b \le b_{max} \\ c_{min} \le c \le c_{max} \\ d_{min} \le d \le d_{max} \end{cases} \tag{19}$$

In Eq. (18), the summation covers the N experimental cutting conditions. F_{FEM} and F_{EXP} denote, respectively, the main cutting force predicted by the finite element model and the measured value for the same cutting condition. The resulting mean squared relative deviation is represented by the fitness value E.

The search history obtained during parameter identification is plotted in Fig. 6. Most of the reduction

in E occurred during the earlier generations, after which the curve became progressively flatter. Continuing the calculation to the 800th generation produced no meaningful further decrease in the objective value. The parameter set retained for the complete coupled variable-friction model was therefore a = 0.042644, b = 1.4576× 10^{-4}, c = 0.86322, and d = 0.08142.

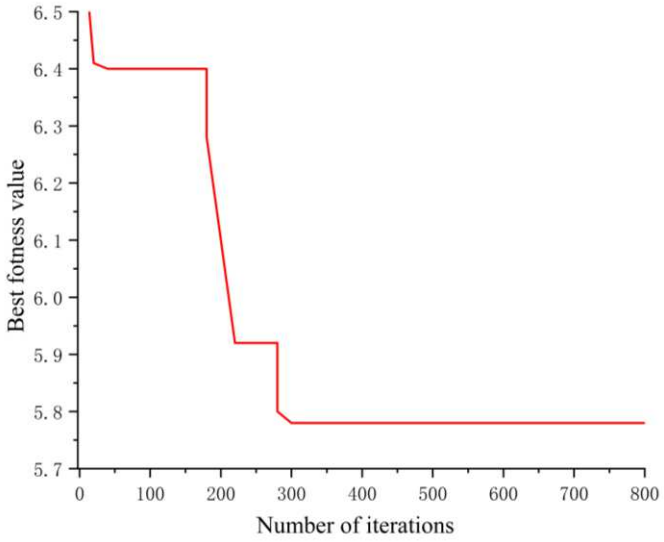


Fig. 6 Convergence curve of the fitness function

4.3 Experimental Validation of the Coupled Variable Friction Model

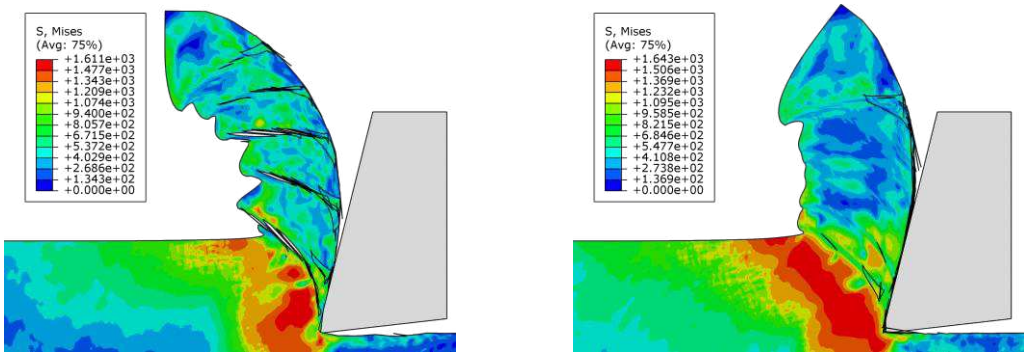
Model performance was examined by comparing the coupled variable-friction formulation with the experimental measurements and with a conventional Coulomb model using a constant friction coefficient of 0.3[34]. Two responses were considered: the main cutting force and the resulting chip morphology.

4.3.1 Comparative Analysis of Cutting Forces

Fig. 7 presents the von Mises equivalent stress fields obtained from the Coulomb and coupled variable-friction models for v=100 m/min and f=0.25 mm/rev. The corresponding main cutting-force histories are given in Fig. 8. A clear difference is visible in the simulated cutting response. With the constant Coulomb coefficient, the chip remained predominantly ribbon-like, whereas the coupled formulation produced a serrated shape associated with the thermal-softening and thermoplastic-instability mechanisms of Ti6Al4V. The force signal from the coupled model also fluctuated around a level closer to the measured force.

The comparison was extended to the three cutting speeds at the same feed rate, as summarized in Fig. 9. Averaging the relative deviations from the experimental measurements gave an error of 20.8% for the

Coulomb formulation and 5.55% for the coupled variable-friction formulation. Thus, for the cutting conditions examined here, updating friction according to the local interface state produced a substantially closer force response than prescribing μ=0.3 over the complete contact zone. Across the investigated cutting conditions, both the experimental measurements and numerical predictions showed a systematic decrease in the main cutting force with increasing cutting speed. The finite element results simultaneously indicated higher temperatures in the primary shear zone and along the tool-chip interface at elevated cutting speeds, suggesting an enhanced contribution of thermal softening. The resulting reduction in the local deformation resistance of Ti6Al4V provides a mechanistic explanation for the lower cutting-force levels observed at higher cutting speeds.



（a）Variable Friction Coefficient Model　　（b）Coulomb Friction Model

Fig. 7 Comparison of the von Mises stress between the Coulomb friction model and the variable friction coefficient model

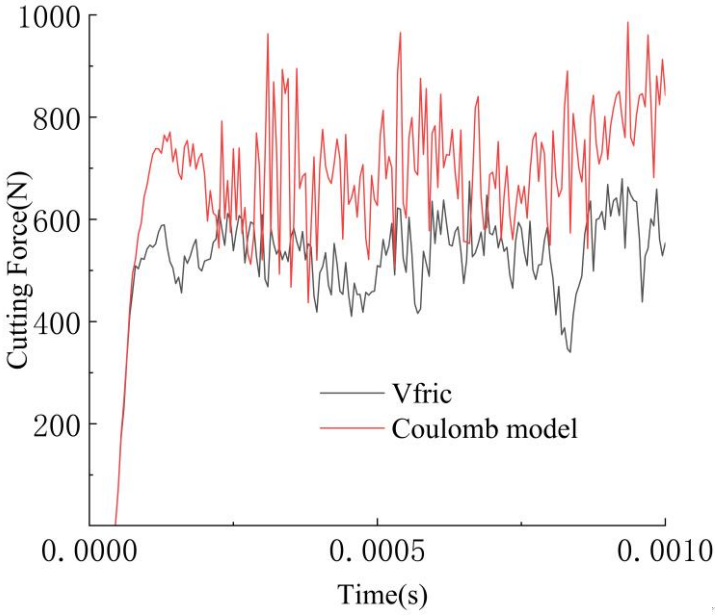


Fig. 8 Cutting force-time curves

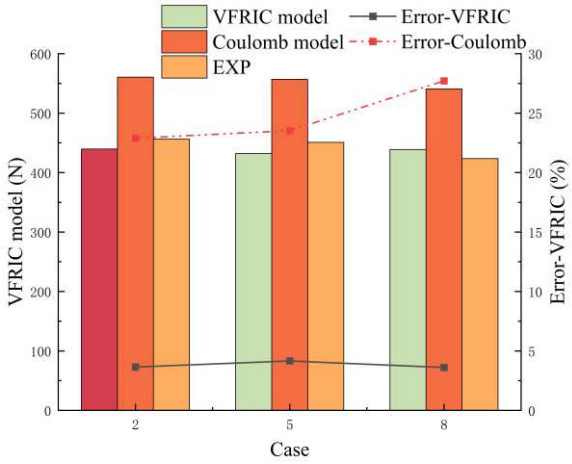
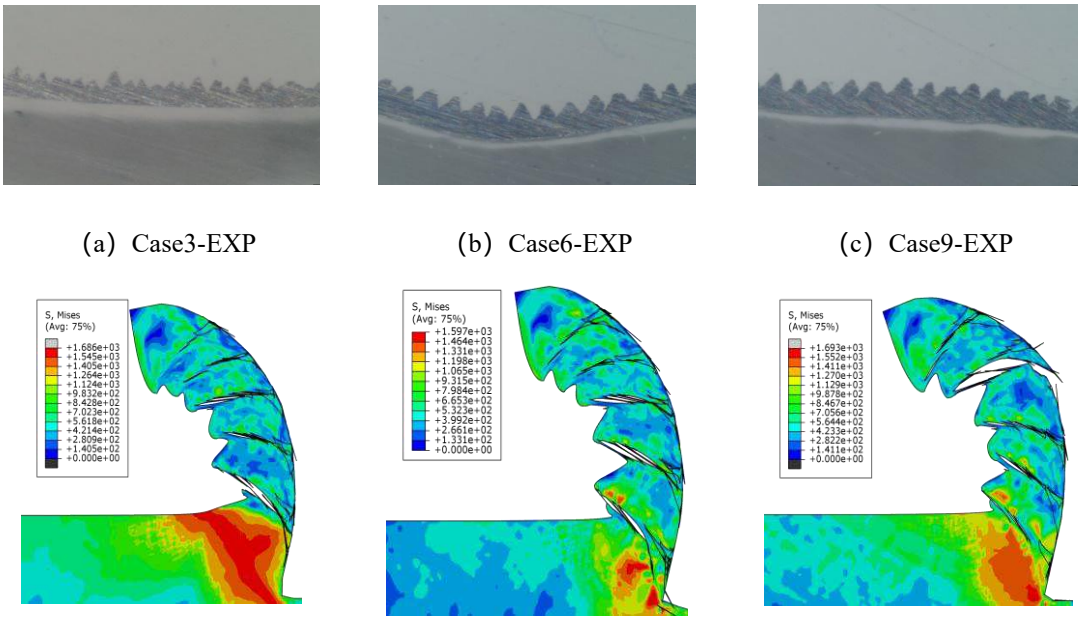


Fig. 9 Comparison of the predicted main cutting forces obtained using different friction models

4.3.2 Comparative Analysis of Chip Morphology

Chips produced in the cutting tests were collected at the different cutting speeds and embedded by cold mounting to prepare cross-sectional specimens. Their profiles were recorded using an industrial camera and a microscope. For comparison, chip shapes were also obtained from simulations using the Coulomb and coupled variable-friction models. The experimental and numerical results are presented in Fig. 10. Periodic serrations were evident in the experimentally obtained chips. A similar segmented pattern appeared in the results from the coupled variable-friction model, while the Coulomb simulation mainly produced an irregular ribbon-like chip. The comparison therefore indicates that allowing friction to change with the evolving contact state improves the numerical reproduction of the serrated-chip behavior associated with shear localization in Ti6Al4V cutting.



(a) Case3-EXP (b) Case6-EXP (c) Case9-EXP

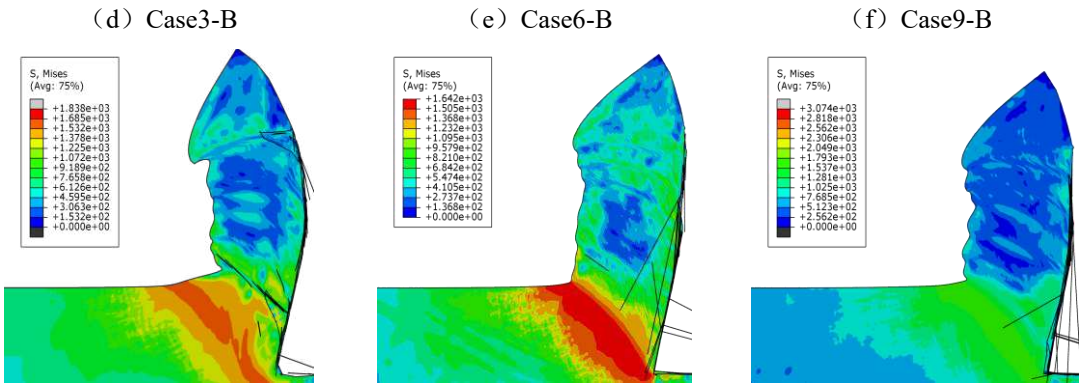


Fig. 10 Comparison of chip morphology at different cutting speeds

To quantitatively assess the capability of the coupled variable-friction model to predict the chip morphology of Ti6Al4V, geometric parameters were introduced to characterize the chip serration degree [39]:

$$G_s = \frac{H - h}{H} \tag{20}$$

where G_S is the chip serration degree. For each serration, H is measured from the chip bottom layer to the tooth peak, whereas h is measured from the same reference layer to the adjacent tooth valley. Three representative serrations were selected from regions in which the segmented profile was relatively stable. The measured H and h values were averaged before calculating G_S. Fig. 11 shows the resulting experimental and numerical serration degrees. In both cases, G_S increased with cutting speed. The experimental values changed from approximately 0.4 to 0.6, whereas the coupled model produced values from approximately 0.3 to 0.5. Across the investigated conditions, the mean difference between simulation and experiment was 19.33%, with the largest deviation occurring for the sixth cutting condition. The larger discrepancy at this condition is associated with the more rapid evolution of the deformation process at elevated cutting speed. The serration period becomes shorter while strain rate and temperature rise more rapidly in the primary deformation zone. Because Ti6Al4V retains heat locally, this temperature increase strengthens thermal softening and alters material flow during shear-band development. In the coupled formulation, temperature also changes the friction boundary condition at the rake face. The chip shape is therefore governed by the combined response of material deformation and interface friction, which explains why the coupled model reproduces the measured segmentation more closely than the constant-friction formulation.

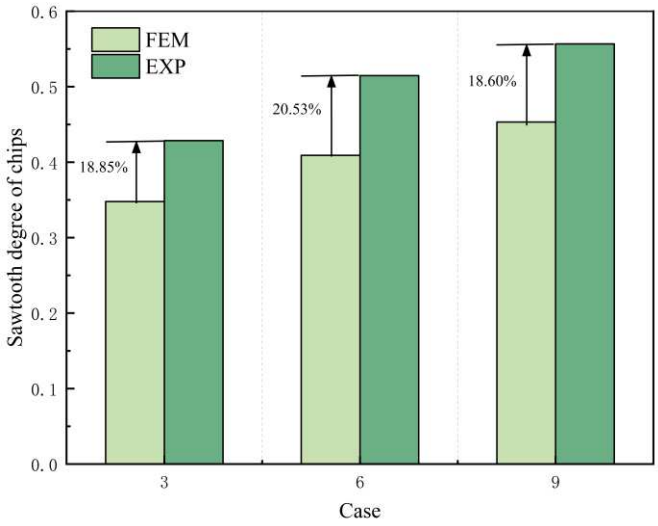


Fig. 11 Comparison of chip serration degree between experiment and simulation

5. Factor Decomposition of the Coupled Friction Model and Analysis of Cutting Responses

The validation in Section 4 establishes the overall performance of the complete friction law but does not distinguish the contribution of each state variable. A factor-decomposition analysis was therefore performed using Model-Full as the reference configuration. Three reduced formulations were generated, each suppressing one explicit dependence—contact temperature, normal contact stress, or relative sliding velocity—while leaving the remaining numerical model unchanged. The same material definition, tool geometry, cutting conditions, and computational settings were used for all simulations. Differences between the reduced models, Model-Full, and the experimental responses were then used to determine how removal of each term affected force prediction and chip formation.

5.1 Construction and Parameter Identification of Single-Factor Ablation Models

5.1.1 Temperature-Term Ablation Model (Model-NoT)

The contribution of explicit temperature sensitivity to the interfacial friction law was isolated by removing the corresponding temperature-dependent factor from the complete formulation. This factor was therefore assigned a value of unity, defining the reduced model Model-NoT. The modification suppresses the direct temperature dependence of the friction coefficient without altering the transient temperature field

or the thermal-softening response of Ti6Al4V represented by the constitutive model. The resulting ablation form is expressed as follows:

$$\begin{cases} \mu = ae^{-bv}/\sigma^{d} \\ \tau = min(\mu\sigma_n, \tau_{max}) \end{cases} \tag{21}$$

where a, b, and d are model parameters to be identified, with ($0 < d < 1$).

Accordingly, temperature can still modify material deformation and the calculated contact field in Model-NoT, but it no longer changes μ\muμ through an explicit temperature term.

5.1.2 Normal-Contact-Stress-Term Ablation Model (Model-Noσ)

The role of normal-contact-stress sensitivity was isolated by suppressing the corresponding ter m in the complete friction formulation. Specifically, the stress-dependent exponent was fixed at (d = 0), defining the reduced model Model-Noσ. Under this condition, the friction coefficient remains governed by contact temperature and relative sliding velocity, while its explicit dependence on nor mal contact stress is removed. The resulting ablation form is given as follows:

$$\begin{cases} \mu = ae^{-bv}\left[1 - \left(\frac{T}{T_m}\right)^{c}\right] \\ \tau = min(\mu\sigma_n, \tau_{max}) \end{cases} \tag{22}$$

where a, b, and c are model parameters to be identified.

Model-Noσ removes the dependence whereby the friction coefficient decreases with increasing normal contact stress. Consequently, in the high-contact-stress region near the tool tip, this model may predict a higher friction coefficient than the complete model. By comparing the resulting cutting responses and prediction errors, the influence of normal-contact-stress dependence on the mechanical behavior of the tool-chip interface can be assessed.

5.1.3 Relative-Sliding-Velocity-Term Ablation Model (Model-NoV)

To evaluate the contribution of relative sliding velocity to the coupled friction model, the velocity-dependent exponent in the complete model was set to (b = 0), resulting in the simplified model denoted as Model-NoV. This model assumes that, within the investigated cutting-speed range, the friction coefficient is independent of relative sliding velocity. The resulting simplified friction relationship is expressed as follows:

$$\begin{cases} \mu = a\left[1 - \left(\frac{T}{T_m}\right)^c\right] / \sigma^d \\ \tau = min(\mu\sigma_n, \tau_{max}) \end{cases} \quad (23)$$

where a, c, and d are model parameters to be identified, with $0 < d < 1$.

By suppressing the velocity-dependent contribution, Model-NoV removes the mechanism through which increasing relative sliding velocity reduces the local friction coefficient. The influence of this simplification is expected to become more pronounced as the cutting speed increases, because the interfacial sliding state departs progressively from that represented by the complete model. Under such conditions, the absence of velocity-induced friction reduction can increase the calculated interfacial shear traction and consequently alter the predicted cutting force, temperature field, and chip-segmentation response. The contribution of the relative-sliding-velocity term is therefore evaluated by comparing the prediction errors and cutting responses of Model-NoV with those obtained from the complete formulation over the investigated cutting conditions.

Because the model formulations were modified, the parameter values identified for the complete model could not be directly applied to the three simplified models. Therefore, inverse parameter identification was performed separately for Model-NoT, Model-Noσ, and Model-NoV. The identification objective remained the minimization of the discrepancy between the simulated and experimentally measured main cutting forces, and the same co-simulation workflow used for the complete model was adopted. For Model-NoT, the identified values of a, b, and d were 0.044082, 4.15677×10^{-5}, and 0.024276, respectively. For Model-Noσ, the identified values of a, b, and c were 0.044256, 8.1991×10^{-5}, and 0.018492, respectively. For Model-NoV, the identified values of a, c, and d were 0.44886, 0.45842, and 0.027077, respectively.

5.2 Effects of Different Friction Factors on the Prediction of Cutting Responses

5.2.1 Effects of Different Friction Factors on the Prediction of Cutting Forces

The three simplified friction laws were individually implemented using VFRIC subroutines and incorporated into the Abaqus finite element model. To ensure a consistent comparison, all models employed the workpiece material properties, tool geometry, cutting parameters, and computational settings described in Section 3. The main cutting forces predicted at the same feed rate but at different cutting speeds were extracted, and the prediction errors of the three simplified models relative to the experimental

measurements were calculated. The results are presented in Fig. 12.

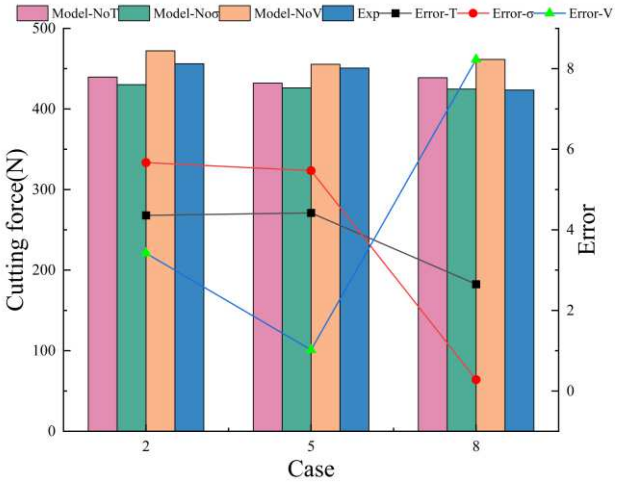


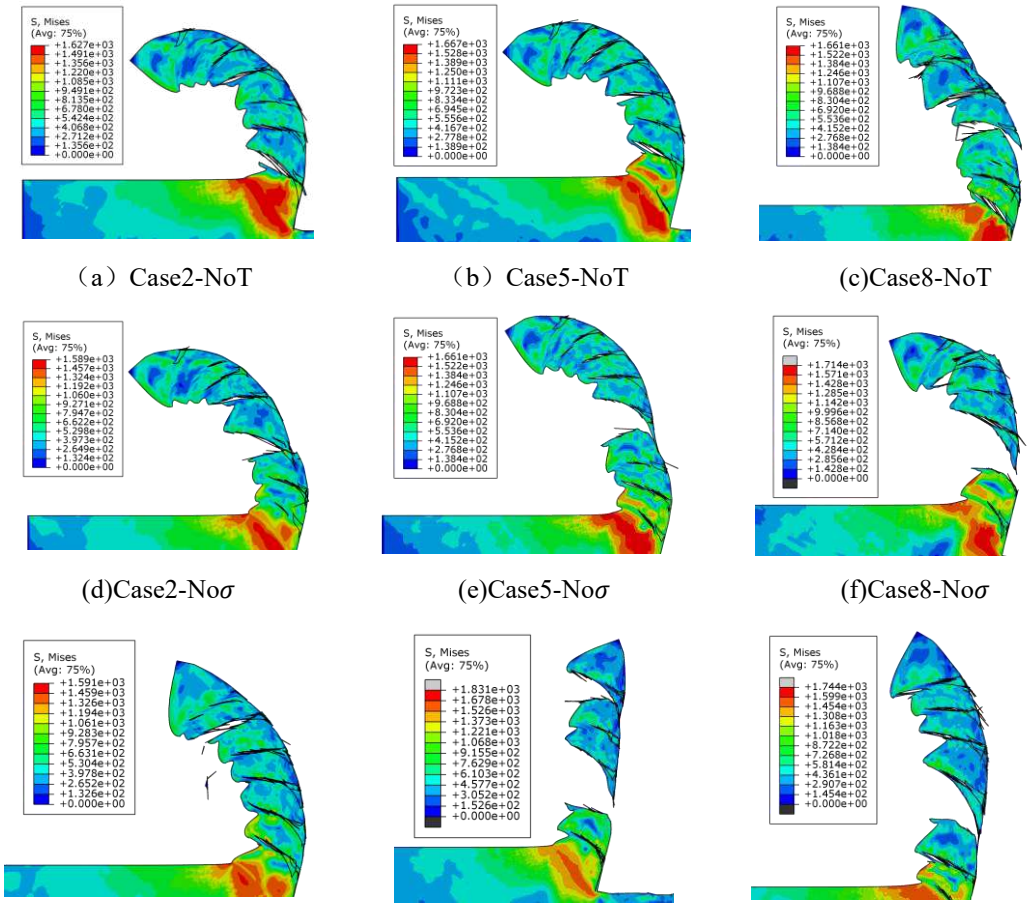
Fig. 12 Comparison of predicted main cutting forces and errors among different models

A clear separation among the three ablation cases is obtained in Fig. 12. Removing the sliding-velocity dependence produces the largest change in the force response. In particular, Model-NoV increasingly exceeds the experimental force as the cutting speed rises. The difference can be traced to the interface law: without the velocity term, the reduction in μ associated with faster local sliding is absent, so a larger shear traction is maintained over the contact region. This effect becomes increasingly visible in the predicted main cutting force at the higher speeds.

Removing the normal-stress dependence produces a smaller change in the overall force magnitude than removing the velocity term. This result concerns the global force response rather than the complete role of normal pressure. The pressure term directly modifies the spatial variation of μ and shear traction along the rake face and can consequently affect quantities that depend more strongly on the local contact state, including interface temperature and chip formation. Within the present cutting conditions, the ablation results therefore identify relative sliding velocity as the dominant friction variable for main-force prediction, while temperature and normal contact stress make additional contributions through the local thermomechanical contact response.

5.2.2 Effects of Different Friction Factors on Chip Morphology and Serration Degree

Following the comparison of the main cutting-force predictions, the chip morphologies predicted by the three simplified models were further examined, as shown in Fig. 13.



（a）Case2-NoT　　（b）Case5-NoT　　(c)Case8-NoT

(d)Case2-Noσ　　(e)Case5-Noσ　　(f)Case8-Noσ

(g)Case2-NoV　　(h)Case5-NoV　　(i)Case8-NoV

Fig. 13 Comparison of chip morphologies predicted by different simplified friction models at various cutting speeds

The chip morphologies in Fig. 13 indicate that all three ablation models retained the capability to reproduce serrated-chip formation, although the predicted segmentation characteristics varied with cutting speed. Model-Noσ generated comparatively well-defined serrations over the three speed levels, whereas larger discrepancies from the experimental chip profiles were observed for Model-NoT and Model-NoV. To quantify these morphological differences, the serration degree was subsequently evaluated, as presented in Fig. 14. The experimental measurements exhibited a progressive increase in serration degree as the cutting speed increased from 60 to 100 m/min. This tendency is consistent with an increasing propensity for localized thermoplastic instability and adiabatic shear localization in Ti6Al4V. Owing to the relatively low thermal conductivity of the alloy, heat generated by severe plastic deformation is not dissipated rapidly from the deformation zone. The resulting local heat accumulation enhances thermal softening and thereby facilitates periodic chip segmentation.

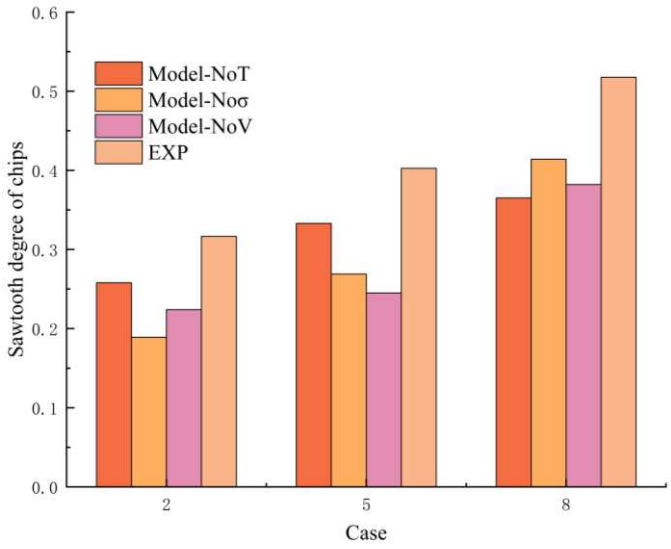


Fig. 14 Comparison of chip serration degree between different simplified models and experiments

All three simplified models predicted serrated chips to some extent; however, their predicted degrees of serration were generally lower than the experimental values. This finding indicates that excluding any of the three influencing factors reduces the model's ability to represent the coupled frictional behavior at the tool-chip interface. Model-Noσ markedly underestimated the degree of chip serration under low-and medium-speed conditions, demonstrating that normal contact stress plays an important role in regulating the local frictional-stress distribution and shear-band formation. Under high-speed conditions, however, its prediction was relatively close to the experimental value, suggesting that thermal softening and strain-rate effects exert a greater influence on chip segmentation during high-speed cutting. Model-NoT exhibited good predictive performance under low and medium-speed conditions, indicating that the thermal-softening behavior incorporated into the material constitutive model can, to some extent, compensate for the absence of explicit temperature dependence in the friction model. Nevertheless, Model-NoV clearly underestimated the degree of chip serration under high-speed conditions. The predictions of Model-NoV were generally lower than the experimental values, with particularly large deviations under medium- and high-speed conditions. These results indicate that relative sliding velocity plays an important role in reducing interfacial friction and governing chip flow and the evolution of periodic shear bands.

The chip results provide a different perspective from the force comparison. No single ablation reproduces the complete response over the full cutting-speed range, indicating that chip segmentation depends on several parts of the interface law. The velocity term becomes particularly important as sliding motion increases, whereas the temperature term links the friction boundary condition with the strong thermal response of Ti6Al4V. Normal contact stress has a smaller effect on the global force but changes

how frictional traction is distributed over the rake face. The agreement obtained with Model-Full is therefore associated with the simultaneous evolution of these mechanisms rather than with one state variable acting independently.

6. Conclusions

A coupled variable-friction model was established for the Ti6Al4V tool-chip interface by incorporating the effects of contact temperature, normal contact stress, and relative sliding velocity. The model was implemented in a two-dimensional orthogonal-cutting simulation through the Abaqus VFRIC subroutine, and its parameters were determined by inverse identification within an Abaqus-Python-Isight co-simulation framework. Its predictive performance and the contributions of the three state variables were evaluated using cutting experiments, a conventional Coulomb friction model, and three single-factor ablation models. The main findings are as follows:

(1) Inverse identification yielded a = 0.042644, b = 1.4576× 10^{-4}, c = 0.86322, and d = 0.08142 for Model-Full. The fitness history changed little after the later optimization stages, and extending the search to 800 generations did not produce a meaningful additional reduction in the objective function.

(2) Incorporating the evolving interfacial state substantially improved the prediction of the main cutting force. The coupled variable-friction model produced an average prediction error of 5.55%, compared with 20.8% for the Coulomb friction model. This reduction indicates that allowing friction to respond to local thermomechanical conditions provides a more accurate representation of the tool-chip interaction than a constant friction coefficient.

(3) Model-Full also reproduced the segmented chip form observed experimentally. The measured serration degree covered approximately 0.4–0.6, compared with approximately 0.3–0.5 in the simulations, giving a mean deviation of 19.33%. Both data sets exhibited stronger segmentation as cutting speed increased.

(4) The ablation calculations separated the roles of the three interface variables. Suppressing the sliding-velocity term caused the largest deterioration in main-force prediction, particularly at higher speeds. Temperature affected both material softening and the friction boundary condition, whereas the normal-stress term mainly redistributed the local frictional state along the rake face. The complete formulation benefits from retaining all three dependencies because they influence different aspects of the

cutting response.

Future work should extend the present two-dimensional orthogonal-cutting framework to three-dimensional simulations incorporating tool wear, so that the coupled evolution of contact temperature, normal contact stress, and relative sliding velocity can be examined under more realistic machining conditions. Independent cutting conditions should also be introduced for model validation, together with multi-objective parameter-identification strategies, to evaluate the robustness and uniqueness of the identified parameters and to further assess the applicability of the model to different workpiece materials and cutting regimes.

References:

[1] Courbon C, Pusavec F, Dumont F, Rech J, Kopac J (2013) Tribological behaviour of Ti6Al4V and Inconel718 under dry and cryogenic conditions—application to the context of machining with carbide tools. Tribol Int 66:72–82. https://doi.org/10.1016/j.triboint.2013.04.010

[2] Moufki A, Molinari A (2005) A new thermomechanical model of cutting applied to turning operations. Part II. Parametric study. Int J Mach Tools Manuf 45(2):181–193. https://doi.org/10.1016/j.ijmachtools.2004.07.005

[3] Liu S, Zhang H, Zhao L, Li G, Zhang C, Zhang J et al (2021) Coupled thermo-mechanical sticking-sliding friction model along tool-chip interface in diamond cutting of copper. J Manuf Process 70:578–592. https://doi.org/10.1016/j.jmapro.2021.09.012

[4] Malakizadi A, Hosseinkhani K, Mariano E, Ng EG, Del Prete A, Nyborg L (2017) Influence of friction models on FE simulation results of orthogonal cutting process. Int J Adv Manuf Technol 88(9–12):3217–3232. https://doi.org/10.1007/s00170-016-9023-4

[5] Afrasiabi M, Saelzer J, Berger S, Iovkov I, Klippel H, Röthlin M et al (2021) A numerical-experimental study on orthogonal cutting of AISI 1045 steel and Ti6Al4V alloy: SPH and FEM modeling with newly identified friction coefficients. Metals 11(11):1683. https://doi.org/10.3390/met11111683

[6] Zhou Z, Wang Y, Xia Z (2025) A novel activated sticking-sliding friction model along tool-chip interface and mechanism analysis in high-speed machining of Ti6Al4V. Proc Inst Mech Eng Part J J Eng Tribol 239(3):339–348. https://doi.org/10.1177/13506501241284321

[7] Liang X, Liu Z, Chen L, Hao G, Wang B, Cai Y et al (2020) Tool wear induced modifications of plastic flow and deformed material depth in new generated surfaces during turning Ti6Al4V. J Mater Res Technol 9(5):10782–10795. https://doi.org/10.1016/j.jmrt.2020.07.093

[8] Zhang C, Choi H (2021) Study of segmented chip formation in cutting of high-strength lightweight alloys. Int J Adv Manuf Technol 112:2683–2703. https://doi.org/10.1007/s00170-020-06057-4

[9] Coulomb CA (1821) Théorie des machines simples: en ayant égard au frottement de leurs parties et à la roideur des cordages. Nouvelle éd. Bachelier, Paris. https://doi.org/10.14711/spcol/b668151

[10] Shi G, Deng X, Shet C (2002) A finite element study of the effect of friction in orthogonal metal cutting. Finite Elem Anal Des 38(9):863–883. https://doi.org/10.1016/S0168-874X(01)00110-X

[11] Molinari A, Moufki A (2005) A new thermomechanical model of cutting applied to turning operations. Part I. Theory. Int J Mach Tools Manuf 45(2):166–180. https://doi.org/10.1016/j.ijmachtools.2004.07.004

[12] Bahi S, Nouari M, Moufki A, El Mansori M, Molinari A (2012) Hybrid modelling of sliding–sticking zones at the tool–chip interface under dry machining and tool wear analysis. Wear 286–287:45–54. https://doi.org/10.1016/j.wear.2011.05.001

[13] Fezai N, Chaabani L, Niang NF, Bin Haamsir MH, Fontaine M, Gilbin A et al (2022) Characterization of friction for the simulation of multi-pass orthogonal micro-cutting of 316L stainless steel. Procedia CIRP 108:845–850. https://doi.org/10.1016/j.procir.2022.03.130

[14] Yin W, Duan C, Li Y, Miao K (2021) Modelling of tool flank–workpiece interface friction considering temperature gradient and particle property for cutting SiCp/Al composites. J Mater Process Technol 298:117302. https://doi.org/10.1016/j.jmatprotec.2021.117302

[15] Wang Q, Lu C, Ye GG, Dai LH (2015) Modelling the tuned criticality in stick-slip friction during metal cutting. Model Simul Mater Sci Eng 23(5):055013. https://doi.org/10.1088/0965-0393/23/5/055013

[16] Saini A, Jayal AD (2019) A predictive model to estimate tool-chip friction in orthogonal machining. Procedia CIRP 82:130–135. https://doi.org/10.1016/j.procir.2019.04.058

[17] Merchant ME (1944) Basic mechanics of the metal-cutting process. J Appl Mech 11(3):A168–A175.

https://doi.org/10.1115/1.4009380
[18] Bowden FP, Tabor D (1942) Mechanism of metallic friction. Nature 150:197–199. https://doi.org/10.1038/150197a0
[19] Mróz Z, Stupkiewicz S (1998) Constitutive model of adhesive and ploughing friction in metal-forming processes. Int J Mech Sci 40(2–3):281–303. https://doi.org/10.1016/S0020-7403(97)00055-6
[20] Puls H, Klocke F, Lung D (2014) Experimental investigation on friction under metal cutting conditions. Wear 310(1–2):63–71. https://doi.org/10.1016/j.wear.2013.12.020
[21] Özel T (2006) The influence of friction models on finite element simulations of machining. Int J Mach Tools Manuf 46(5):518–530. https://doi.org/10.1016/j.ijmachtools.2005.07.001
[22] Lučić M, Nedić B, Marušić V, Baralić J, Mitrović A (2020) Numerical analysis of the temperature field in the cutting zone in continuous and discontinuous metal cutting by turning. Teh Vjesn 27(5):1486–1491. https://doi.org/10.17559/TV-20190612173031
[23] Komanduri R, Hou ZB (2002) On thermoplastic shear instability in the machining of a titanium alloy (Ti6Al4V). Metall Mater Trans A 33:2995–3010. https://doi.org/10.1007/s11661-002-0284-1
[24] Zhang Y, Mabrouki T, Nelias D, Gong Y (2011) FE-model for titanium alloy (Ti6Al4V) cutting based on the identification of limiting shear stress at tool-chip interface. Int J Mater Form 4:11–23. https://doi.org/10.1007/s12289-010-0986-7
[25] Zou Z, Zhang T, He L, Zhao X, Zhou T (2024) Hybrid modeling prediction of residual stresses in turned Ti6Al4V considering frictional contact. J Mater Res Technol 30:4377–4392. https://doi.org/10.1016/j.jmrt.2024.04.157
[26] Wang Y, Li J, Liu K et al (2022) Experiment and numerical study of chip formation mechanism during cryogenic machining of Ti6Al4V alloy. J Manuf Process 84:1246–1257. https://doi.org/10.1016/j.jmapro.2022.10.020
[27] Liang X, Liu Z, Wang B, Hou X (2018) Modeling of plastic deformation induced by thermo-mechanical stresses considering tool flank wear in high-speed machining Ti6Al4V. Int J Mech Sci 140:1–12. https://doi.org/10.1016/j.ijmecsci.2018.02.031
[28] Yaich M, Ayed Y, Bouaziz Z, Germain G (2017) Numerical analysis of constitutive coefficients effects on FE simulation of the 2D orthogonal cutting process: application to the Ti6Al4V. Int J Adv Manuf Technol 93:283–303. https://doi.org/10.1007/s00170-016-8934-4
[29] Liu M, Li G, Zhao S, Wang F, Li L, Cai Y et al (2025) Identification of heterogeneous constitutive model of laser additive manufactured materials based on nano-indentation test and orthogonal metal cutting. J Mater Res Technol 34:58–76. https://doi.org/10.1016/j.jmrt.2024.12.041
[30] Zerilli FJ, Armstrong RW (1987) Dislocation-mechanics-based constitutive relations for material dynamics calculations. J Appl Phys 61(5):1816–1825. https://doi.org/10.1063/1.338024
[31] Bodner SR, Partom Y (1975) Constitutive equations for elastic-viscoplastic strain-hardening materials. J Appl Mech 42(2):385–389. https://doi.org/10.1115/1.3423586
[32] Paturi UMR, Narala SKR, Pundir RS (2014) Constitutive flow stress formulation, model validation and FE cutting simulation for AA7075-T6 aluminum alloy. Mater Sci Eng A 605:176–185. https://doi.org/10.1016/j.msea.2014.03.033
[33] Umbrello D (2008) Finite element simulation of conventional and high speed machining of Ti6Al4V alloy. J Mater Process Technol 196(1–3):79–87. https://doi.org/10.1016/j.jmatprotec.2007.05.007
[34] Mustafa M, Pervaiz S, Deiab I (2024) The effect of rake angle and cutting edge radius on the orthogonal cutting process of Ti6Al4V alloy. Recent Prog Mater 6(2):013. https://doi.org/10.21926/rpm.2402013
[35] Yameogo D, Haddag B, Makich H, Nouari M (2019) A physical behavior model including dynamic recrystallization and damage mechanisms for cutting process simulation of the titanium alloy Ti6Al4V. Int J Adv

Manuf Technol 100:333–347. https://doi.org/10.1007/s00170-018-2663-9
[36] Johnson GR, Cook WH (1985) Fracture characteristics of three metals subjected to various strains, strain rates, temperatures and pressures. Eng Fract Mech 21(1):31–48. https://doi.org/10.1016/0013-7944(85)90052-9
[37] Hancock JW, Mackenzie AC (1976) On the mechanisms of ductile failure in high-strength steels subjected to multi-axial stress-states. J Mech Phys Solids 24(2–3):147–160. https://doi.org/10.1016/0022-5096(76)90024-7
[38] Soliman HA, Shash AY, El-Hossainy TM, Abd-Rabou M (2020) Cutting forces and crater wear prediction in orthogonal cutting using two approaches of finite element modeling. Eng Rep 2(10):e12240. https://doi.org/10.1002/eng2.12240
[39] Schulz H, Abele E, Sahm A (2001) Material aspects of chip formation in HSC machining. CIRP Ann 50(1):45–48. https://doi.org/10.1016/S0007-8506(07)62067-8

Statements and Declarations Funding

This work was supported by the 2026 National Natural Science Foundation Incubation Project of Guizhou Normal University (Grant No. 2026-07), the Guizhou Provincial Science and Technology Program (Platform Research Project), Subproject “Key Technologies for Precision Machining of Aeronautical Structural Components” (Grant No. CXPTXM[2025]008), and the 2025 Guizhou Provincial Science and Technology Support Program, “Preparation Technology and Application of Copper-Steel Bimetal for Next-Generation Aviation Hydraulic Pumps” (Grant No. [2025]043).

Competing Interests

The authors have no relevant financial or non-financial interests to disclose.

Author Contributions

Chengsong Ma: Writing-review & editing, Writing-original draft, Visualization, Validation, Supervision, Resources, Methodology, Inves tigation, Funding acquisition, Formal analysis, Conceptualization. **Xinxin Zhang**: Methodology, Formal analysis, Data curation. **Yang Xin**: Software, Formal analysis. **Zichuan Zou**: Writing-review & editing, Validation, Supervision, Funding acquisi tion, Conceptualization.

Data Availability

Available from the corresponding author upon reasonable request

Supplementary Files

This is a list of supplementary files associated with this preprint. Click to download.

- GraphicalAbstract.pptx